Bollettino di Geofisica Teorica ed Applicata Vol. 58, n. 4, pp. 415-430; December 2017
DOI 10.4430/bgta0198

2D approach for modelling self-potential anomalies: application to synthetic and real data

I. Oliveti and E. Cardarelli

DICEA, University "Sapienza", Roma, Italy

(Received: February 21, 2017; accepted: July 7, 2017)

ABSTRACT The aim of this work is to present a 2D Matlab code based on the finite element method for providing numerical modelling of both groundwater flow and self-potential signals. The distribution of the self-potential is obtained by starting with the solution of the groundwater flow, then computing the source current density, and finally calculating the electrical potential. The reliability of the algorithm is tested with synthetic case studies in order to simulate both the electric field resulting from the existence of a leak in the dam and SP signals associated with a pumping test in an unconfined aquifer. In addition, the algorithm was applied to field data for the localization of piping sinkholes. The results show that the outputs of the algorithm yielded satisfactory solutions, which are in good agreement with those of previous studies and field investigations. In details, the synthetic data and SP anomalies calculated by using the code are very close in terms of sign and magnitude, while real data tests clearly indicated that the computed SP signals were found to be consistent with the measured values.

Key words: streaming potential, finite element method, forward modelling, hydrogeology.

1. Introduction

The self-potential (SP) method is a well-established geophysical technique that has been applied, since its inception in the early 19th century, to mineral exploration, oil well logging, geothermal exploration and more recently hydrogeological, environmental and engineering investigations. The renewed interest in this technique gives an understanding of the SP mechanism new importance.

In many cases, the SP method has been mainly used in qualitative analysis of the measured data. Recent efforts in this field have also attempted to provide a quantitative interpretation of SP anomalies. Many methods of interpretation were developed for SP data such as geometric source techniques, imaging methods, forward modelling and inversion.

Geometric source techniques, originally utilized to infer the locations of SP anomalies associated with ore bodies, are based on the assumption that the sources may be approximated by a polarized model of simple geometry. Curve-matching (Meiser, 1962), parametric curve (Bhattacharya and Roy, 1981), inverse methods (Abdelrahman *et al*., 2003) and non-conventional procedures (e.g., Eppelbaum *et al*., 2001, 2004) have been used to recover source parameters such as the surface location, depth, geometry and dip or polarization angle of the body.

Source image methods are applied to reconstruct the most probable location and shape of

© 2017 – OGS

discrete SP buried sources, by estimating the position of their centres and critical points of their boundaries, as corners, wedges and vertices. These methods assume that measured SP data result from the aggregation of poles, dipoles, quadrupoles and octopoles in the subsurface, and, consequently, must employ normalized cross-correlation to enable a comparison of sources at different depths (Iuliano *et al*., 2002).

Within the framework of numerical approaches, the conventional and extended Euler deconvolution has been used to determine location, depth and geometry of the causative source. Shape factor, depth and polarization angle for simple geometries of source models have been also estimated by sophisticated optimization methods, such as genetic algorithms (Abdelazeem and Gobashy, 2006), particle swarm optimization (Pekşen *et al*., 2011) and very fast simulated annealing (Srivastava and Sen, 2009).

Other methods are based on the continuous wavelet transform, which allows the characterization of discontinuities or abrupt changes in the measured signal and a quick analysis of potential field data (Fedi *et al*., 2010).

The inversion of SP data provides a more rigorous means of interpreting a subsurface distribution of current sources. Shi (1998) developed an inversion method for 3D SP which requires a priori information to improve the robustness of the solution. Minsley (2007) further developed this inverse procedure by introducing sensitivity scaling and constraints. They performed an inversion of SP data to define the shape and extension of a contaminant plume where redox processes are occurring. Linde and Revil (2007) solved the Poisson equation to determine the distribution of the redox potential versus depth over a contaminant plume associated with the presence of a municipal landfill. Mendonça (2008) developed an algorithm to invert SP signals to delineate the position of ore bodies at depth using the geobattery model developed by Stoll *et al*. (1995). Soueid Ahmed *et al*. (2013) introduced a finite element algorithm for localizing the causative source of SP signals associated with ground water flow. All these models generally include the distribution of the electrical resistivity as prior information in the inversion process.

Formulating an efficient inversion algorithm requires the knowledge of the forward modelling algorithms for the problem of interest. Forward modelling methods have been developed to predict the SP response to a primary fluid flow field. Sill (1983) was the first to introduce a physics-based approach to simulate numerically the occurrence of SP anomalies associated with ground water flow, using the finite-difference method. Later, the streaming potential problem has been solved with the finite element approach (Jardani *et al*., 2006a) and the finite volume approach (Sheffer and Oldenburg, 2007).

This work aims to further extend the SP technique to the quantitative estimation of streaming potential distributions, creating a two dimensional finite-element forward algorithm to be used for various saturated flow problems of complex geometry in engineering and hydrogeological applications.

The reliability of the algorithm is tested by comparison of the results with those obtained by other authors on synthetic models.

Finally, we present a field data example related to the reconstruction of the SP anomalies resulting from the groundwater flow through a piping sinkhole located in the San Vittorino Plain, a sinkhole prone area of the central Italy crossed by the Velino River. The SP signals determined at the ground surface using the finite element model are compared with the SP measurements performed by Cardarelli *et al*. (2014) on the same profile.

2. From theory to forward modelling

Streaming potentials result from the coupling between fluid flow and electrical conduction in porous media, a phenomenon known as the electrokinetic effect (Ishido and Mizutani, 1981). In the absence of significant chemical concentration or temperature gradients, the coupled flow equations that describe electrokinetic processes in a water-saturated medium heterogeneous are (Sill, 1983):

$$\Gamma_i = -L_i \nabla\Phi_i - L_{ij} \nabla\Phi_j \qquad \textit{Coupled hydraulic flow} \qquad (1)$$

$$\Gamma_j = -L_{ji} \nabla\Phi_i - L_j \nabla\Phi_j \qquad \textit{Coupled electrical flow} \qquad (2)$$

where the L are phenomenological coupling coefficients that link the forces $\nabla\Phi$ to fluxes Γ. The term $-L_{ij} \cdot \nabla\Phi_j$ describes electro-osmotic fluid flow due to the viscous drag of the pore water associated with the displacement of the excess of electrical charge in an electrical field while $-L_{ji} \cdot \nabla\Phi_i$ describes streaming current flow due to the drag of the electrical excess charge contained in the electrical diffuse layer. These phenomena are connected through the Onsager reciprocal relations, which state that $L_{ij} = L_{ji}$ (Onsager, 1931).

The gradient terms are considered thermodynamic forces and must be formulated to uphold the principles of non equilibrium thermodynamics (de Groot, 1951). The most common form of the coupled flow equations reported in the literature express the hydraulic gradient in terms of pressure P (Pa), such that $\nabla P = \rho_w g \cdot \nabla h$, where ρ_w denotes the mass density of the pore water (kg/m^3), g denotes the acceleration of the gravity (m/s^2) and h the hydraulic head (m). Using this convention, the coupled flow relations take the form of Eqs. 3 and 4, where L_{ji} in terms of a pressure gradient becomes $L_{\nabla P} = \frac{L_{ji}}{\rho_w}$(A · s^2/kg) while L_{ij} assumes the form of the coefficient of electroosmotic permeability $k_e = \frac{L_{ij}}{\rho_w}$ (m^2/s · V).

$$\mathbf{u} = -\frac{k}{\mu}\nabla P - k_e \nabla\psi \qquad (3)$$

$$\mathbf{J} = -L_{\nabla P} \nabla P - \sigma\nabla\psi \qquad (4)$$

In the formulation described above **J** is the electrical current density (A/m^2), **u** is the seepage velocity (m/s^2) (Darcy velocity), $-\nabla\psi$ is the electrical field in the quasi-static limit of the Maxwell equations (A/m^2), σ and k are the electrical conductivity (S/m) and intrinsic permeability (m^2) of the porous medium, respectively, and μ is the dynamic shear viscosity of the pore water (Pa×s).

The alternative formulation to Eq. (4) is (Revil and Linde, 2006):

$$\mathbf{J} = -Q_v \mathbf{u} - \nabla\psi \qquad (5)$$

where Q_v is the excess of charge (of the diffuse layer) per unit pore volume (C/m^3). It can be predicted from the permeability (expressed in m^2) according to $\log_{10} Q_v = -9.2 - 0.82 \log_{10} k$ (Jardani *et al.*, 2007a).

However, if the only component of the electrical field is that produced through the electrokinetic coupling, electroosmotic contribution in Eq. 3 can be safely neglected, so that we recover the Darcy constitutive equation. This is supported by (Mitchell, 1991), who reported negligible contribution of the electroosmotic flow term in materials with hydraulic conductivity greater than 10^{-9} m/s.

The constitutive equations, Eqs. 3 and 5, are completed by two continuity equations for the mass of the pore water and the electrical charge, respectively. The groundwater flow is governed by the diffusion equation (e.g., Bear, 1988):

$$\frac{\partial P}{\partial t} = \nabla \cdot (D \nabla P) \tag{6}$$

where $D = \frac{k}{\mu \beta_s}$ denotes the hydraulic diffusivity (m^2/s) and β_s is the specific storage (1/Pa). It is subjected to the following Dirichlet and Neumann boundary conditions:

$$P = P_D \text{ at } \Gamma_D \qquad -\mathbf{n} \cdot \frac{k}{\mu} \nabla P = 0 \text{ at } \Gamma_N \tag{7}$$

The pressure P_D denotes the pressure fixed at the boundary Γ_D and n is the unit vector normal to the boundary Γ_N.

The continuity equation for the electrical charge is:

$$\nabla \cdot \mathbf{J} = 0 \tag{8}$$

which means that the current density is conservative in the quasi-static limit of the Maxwell equations. Combining Eqs. 5 and 8 gives a Poisson equation with a source term that depends only on the seepage velocity in the ground:

$$\nabla \cdot (\sigma \nabla \psi) = \nabla \cdot \mathbf{J}_s \tag{9}$$

where $\mathbf{J}_s$ is called the streaming current density (A/m^2).

Generally, the Neumann boundary condition Γ_N is imposed at the insulating air-ground interface and a Dirichlet boundary condition Γ_D is established at the others boundaries:

$$\psi = 0 \text{ at } \Gamma_D - \mathbf{n} \cdot (\sigma \nabla \psi - J_s) = 0 \text{ at } \Gamma_N \tag{10}$$

The physical model described above indicates that the source current density responsible for the occurrence of the SP signals is strongly related to the ground water flow pathways (see Revil and Jardani, 2010).

The modelling method is a three-step process. First, Eq. 6 is solved with appropriate (Neuman or Dirichlet) boundary conditions for the pressure or groundwater flow. Then, the current source density is calculated on the basis of previously obtained hydraulic gradient distribution ($\mathbf{J}_s = Q_v \mathbf{u}$). Finally, the SP signals are computed by solving Eq. 9 with appropriate boundary conditions on the electrical potential (Fig. 1).

We developed an interactive interface to call all the functions in order to add geometry, mesh, physics settings, boundary conditions, solvers, post-processing and visualizations. During code execution, the procedure first loads the mesh, which is created in NETGEN, an adaptive mesh

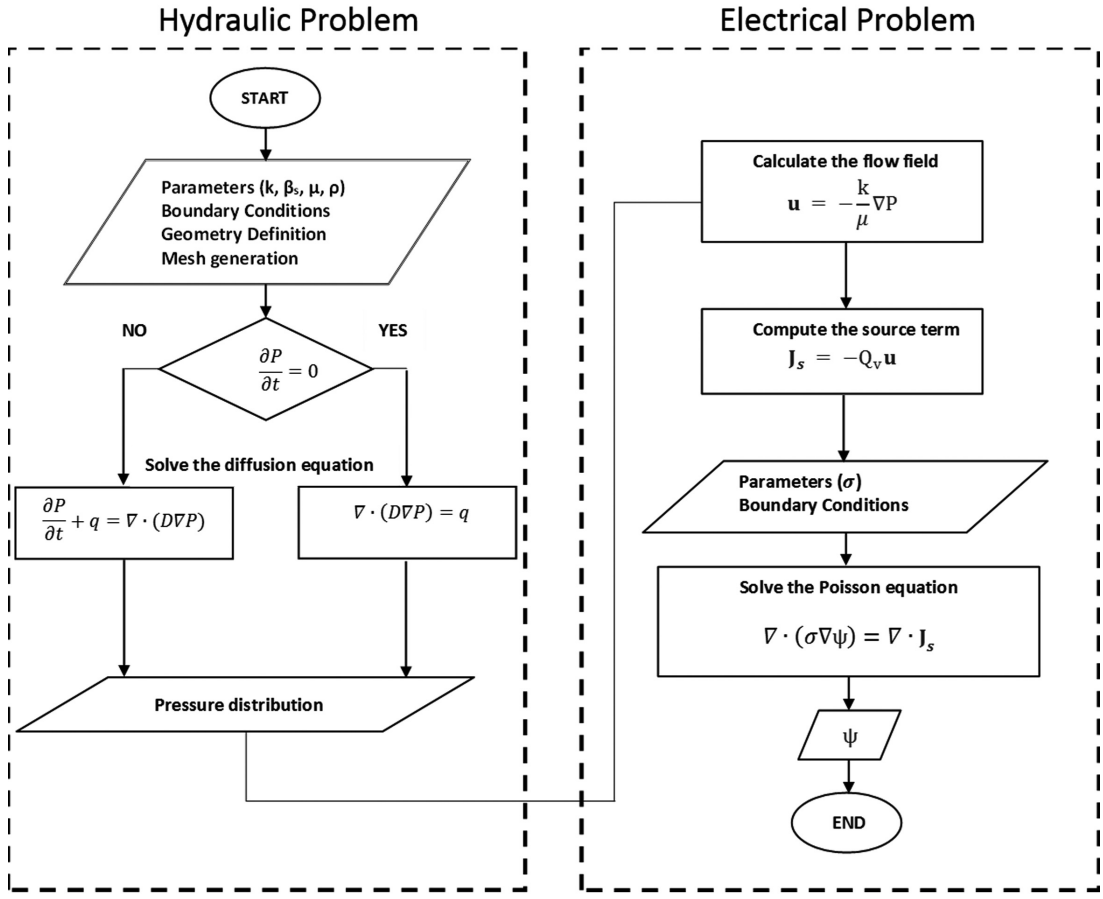

Fig. 1 - Scheme of numerical solution of the forward problem.

generator able to retain an accurate forward solution without drastically increase the number of elements, a huge problem using standard machines with limited local memories (for further details sourceforge.net/projects/netgen-mesher). Next, the designed algorithm requires a priori information in terms of hydraulic and electrical conductivities. Then, the solver is executed for the hydraulic and the electrical problem. Furthermore, it permits to arbitrarily include equations that may describe a material property, boundary, source or sink term, or even a unique set of partial differential equations (PDEs).

In chapter 3, the effectiveness of the algorithm is demonstrate by reanalyzing previously published works. We compared our method with two widely used algorithms. The first is a 2D plus time numerical code called Groundwater Flow Geo-Electrical Mapping (GWFGEM) for hydrogeological purposes based on the finite-difference method. The second one is the commercial software COMSOL Multiphysics.

The main advantage of the proposed approach compared to the first code is that it can be easily adapted to a variety of use cases, not just pumping test experiments. Furthermore, unlike a commercial software, our easy-to-use code can be continuously modified and updated. Nevertheless its simplicity and the need for improvement, it thus provides a useful starting point for implementing an inversion algorithm.

3. Finite element formulation

The previous set of equations (Eqs. 1 to 10) is solved creating a weak formulation, the basis for the finite element discretization.

Multiply Eqs. 6 and 9 by an arbitrary weight function, *w* (*x*, *y*), integrate over an arbitrary domain, Ω, whose boundary is Γ, and apply Green's theorem (Bastos and Sadowski, 2003):

$$\int_{\Omega} \beta_s \frac{\partial P}{\partial t} w = -\int_{\Omega} \frac{k}{\mu} \nabla P \nabla w + \int_{\Gamma} \frac{k}{\mu} \nabla P \mathbf{n}\, w \tag{11}$$

$$\int_{\Omega} \sigma \nabla \psi \nabla w = \int_{\Omega} (\nabla \cdot J_s) w + \int_{\Gamma} \sigma \nabla \psi \mathbf{n}\, w \tag{12}$$

The assumed solution of Eqs. 11 and 12 for an arbitrary, *n-node* element is defined by:

$$P^e(x,y) = \sum_{j=1}^{n} P_j^e \varphi_j^e(x,y) \qquad \psi^e(x,y) = \sum_{j=1}^{n} \psi_j^e \varphi_j^e(x,y) \tag{13}$$

where P_j^e and ψ_j^e are the nodal values for P (x, y) and ψ (x, y), respectively, at node j for the element, and φ_j^e is the interpolation function at node j within the element.

The interpolation functions must satisfy the conditions:

$\varphi_j^e(x_k, y_k) = \delta_{jk}$ at all nodes (j, k) = 1, 2, ..., n and $\Sigma_{j=1}^{n} \varphi_j^e(x,y) = 1$ within Ω.

The Kronecker Delta is defined as:

$\delta_{jk} = 1$ for j = k and

$\delta_{jk} = 0$ for j ≠ k

Because the weight function represents a variation of the primary variables, P (x, y) and ψ (x, y), it takes on the nodal values $w_i = \varphi_i^e$, i = 1, 2, ..., n. On substituting Eqs. 13 into 11 and 12, exchanging the order of integration and summation, for stationarity conditions we obtain the generalized matrix equation:

$$\sum_{j=1}^{n} \mathbf{K_{ij}^e}\, \mathbf{u_j^e} = \mathbf{Q_i^e} \qquad i = 1, 2, \ldots\ldots, n \tag{14}$$

where $\mathbf{K_{ij}^e} = \int_{\Omega} c \left[\frac{\partial \varphi_i^e}{\partial x} \frac{\partial \varphi_j^e}{\partial x} + \frac{\partial \varphi_i^e}{\partial y} \frac{\partial \varphi_j^e}{\partial y} \right] dxdy$, $\mathbf{Q_i^e} = \int_{\Gamma} q_n \varphi_j^e\, ds + \int_{\Omega} f \varphi_i^e dxdy$

with $c = \frac{k}{\mu}$, $q_n = \frac{k}{\mu} \nabla \left(\sum_{j=1}^{n} P_i^e \varphi_i^e \right) \mathbf{n}$ and $f = 0$, for the hydraulic problem

with $c = \sigma$, $q_n = \sigma \nabla \left(\sum_{j=1}^{n} \psi_i^e \varphi_i^e \right) \mathbf{n}$ and $f = \nabla \cdot \mathbf{J}_s$, for the electrical problem

Eq. 14 is solved twice using a Gaussian elimination with partial pivoting. In the first solution, we start from hydraulic boundary conditions and hydraulic conductivity values to obtain the water

pressure distribution. In the second solution, we start from the calculated water pressure, excess of charge per unit pore volume, electrical conductivity and electrical boundary conditions to obtain the SP electrical potential.

4. Synthetic data examples

The finite element code, implemented in Matlab, was tested on two synthetic models. First, we simulated the case of a pumping test in an unconfined aquifer. The model of the test site and details of the experiment were described by Titov *et al*. (2005). The electrical and hydraulic parameters were estimated by the authors and illustrated in Fig. 2 and Table 1: the values of electrical conductivity σ were taken from an electrical resistivity tomographic cross-section while the hydraulic transmissivity T was assumed larger for the first metres from the pumping well than far away and the storativity S was assumed to be constant through the entire aquifer. Taken into account that we used the hydraulic parameters determined by the authors on the basis of the Theis (1935) solution and a trial and error procedure to find the best fit between experimental and synthetic data, we considered the aquifer confined in the course of the pumping test (with the initial head at 48 m above the datum).

Hydraulic heads h in the aquifer were calculated analytically using the solution given by Butler (1988). This solution assumes the pumping well is located at the centre of a disk with radius R embedded within an infinite matrix. Hydraulic properties are assumed uniform within each zone (disk and matrix), but may differ between the two zones such as in this case.

For the hydraulic modelling, MAxSym, a Matlab tool, which is designed specifically to simulate axisymmetric flow (Louwyck *et al*., 2012), was utilized.

In this way, we modelled the pumping phase, keeping fixed the known values of hydraulic parameters. We assessed the consistency of the model by comparing the piezometric levels reconstructed by Titov *et al*. (2005) and our synthetic hydraulic heads (Fig. 3).

Then, we also determined SP signals on the basis of the calculated distribution of hydraulic head and the known electrical conductivity values. We used the no-flow condition on the ground

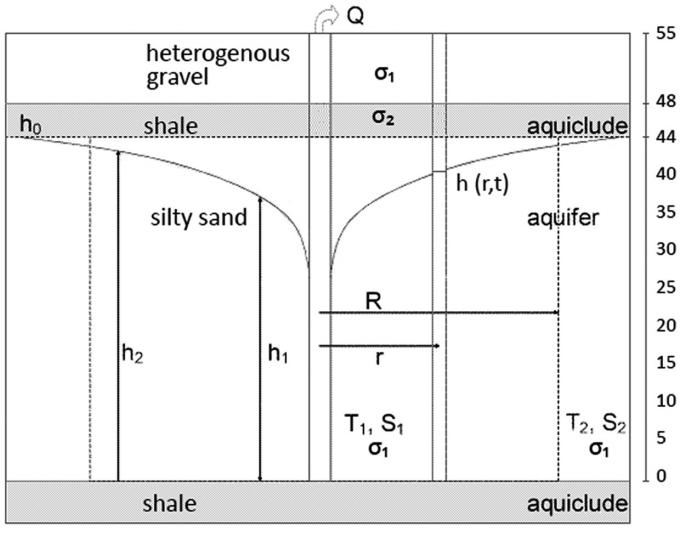

Fig. 2 - Sketch of the pumping test. Petrophysical parameters (T and S are the aquifer transmissivity and storativity, respectively, σ is the electrical conductivity) as well as the initial head distribution h_o = 48 m, and the pumping rate Q = 2.7 L/s are involved into the numerical computations.

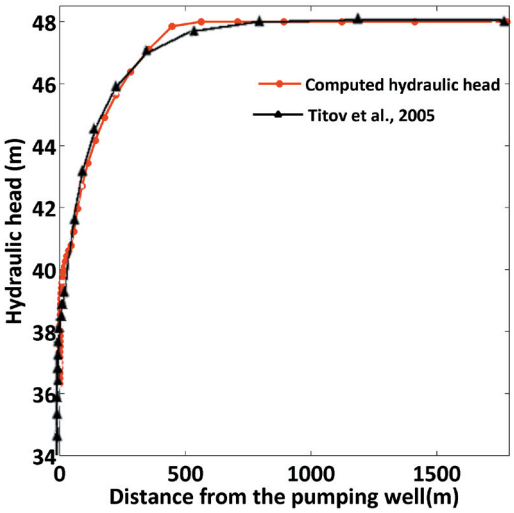

Fig. 3 - Modelled hydraulic head at the end of the pumping phase using MaxSym (red circles) and synthetic data from Titov *et al*., (2005) (black triangles). We note a good agreement between profiles.

Table 1 - Model parameters for the synthetic case study.

Parameters	T (m²/d)		S		σ (S/m)		Radius (m)
	T_1	T_2	S_1	S_2	σ_1	σ_2	R
Model	50	12	$4.8 \cdot 10^{-4}$	$4.8 \cdot 10^{-4}$	10^{-2}	10^{-1}	40

surface and the condition of zero electrical potential on the other boundaries of the aquifer. The right boundary of the model was located far away from the pumping well in order to ensure that the boundary conditions have no influence on the computation of the SP. The potentials were calculated relative to infinite point in the vicinity of the pumping well at the end of the pumping phase (quasi-state condition), when there is a perfectly linear relationship between the SP signals and the hydraulic heads, as is shown in Fig. 4, the positive electrical source is centred on the pumping well, while negative sources are located far away under transient regime of the groundwater flow in accordance with the results obtained by the authors.

A second synthetic case is shown in Fig. 5. We performed the numerical simulation for a synthetic embankment dam reported by Ikard *et al*. (2012). A leakage was reproduced by adding a permeable pipe located inside the dam core that simulates the existence of a preferential ground water flow pathway with permeability much higher than the permeability of the surrounding area. The material properties, we used to run the numerical model, are provided by the authors (Table 2). We chose a high quality triangular mesh denser at the position of the conduit in order to guarantee the accuracy of the forward solver (Fig. 5b).

The SP synthetic data were referenced to a point located at infinity. Boundary conditions were defined as follows: water head pressures were imposed along the lateral boundaries using a Dirichlet condition. At the bottom of the dam and at the ground surface we imposed an insulating boundary condition ($\mathbf{n} \cdot \mathbf{j} = 0$); where $\mathbf{n}$ is the unit vector normal to the ground surface).

For the electrical problem, the Neumann boundary condition was imposed at the air-ground interface while a Dirichlet boundary condition was applied at the other boundaries. The numerical model was performed for steady-state flow conditions. The groundwater flow due to the hydraulic gradient between the upstream and downstream of the dam is illustrated in Fig. 5a. The hydraulic

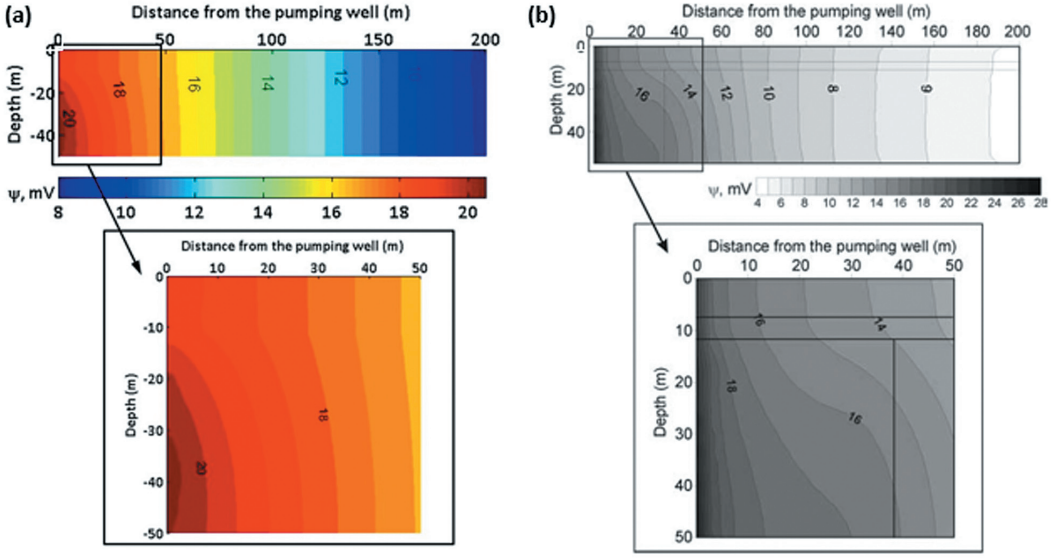

Fig. 4 - Cross-section of the synthetic SP radial distribution around the pumping well (only one side is modelled, because of the symmetry of the problem with an axis of symmetry corresponding to the well): a) streaming potentials obtained by adopting the finite element algorithm; b) computed SP signal from Titov *et al*. (2005).

Table 2 - Model parameters for the synthetic case study.

Parameters	k (m^2)	σ (S/m)	Q_v (C/m^3)
Water	0	7×10^{-2}	0
Bedrock	0	5×10^{-4}	0
Dam	0	5×10^{-4}	0
Leak	2×10^{-8}	7×10^{-3}	1.2×10^{-3}
Seal	0	2×10^{-3}	0

gradient and the average velocity in the conduit resulted around 0.17 and 0.017 m/s, respectively. The simulated SP signals are on the same order of magnitude than those obtained by the authors using a commercial finite element code (COMSOL Multiphysics) (Fig. 6).

The position of the infiltration inlet is characterized by negative SP signals while a positive anomaly denotes the outlet of the flow path and is associated to the divergence of the source current.

5. Field application

Streaming potentials can be used as indicators of the infiltration of the water through soil-filled sinkholes. Previous studies showed that negative SP anomalies over sinkholes are due to the expected electrokinetic effects of groundwater flowing downwards through a conduit. Therefore, recently several works have focused on the use of the SP method to survey sinkholes and karst (Jardani *et al*., 2006b, 2007b; Bumpus and Kruse, 2014). In particular, Cardarelli *et al*. (2014) employed SP method in combination with electrical and seismic tomography for detection of

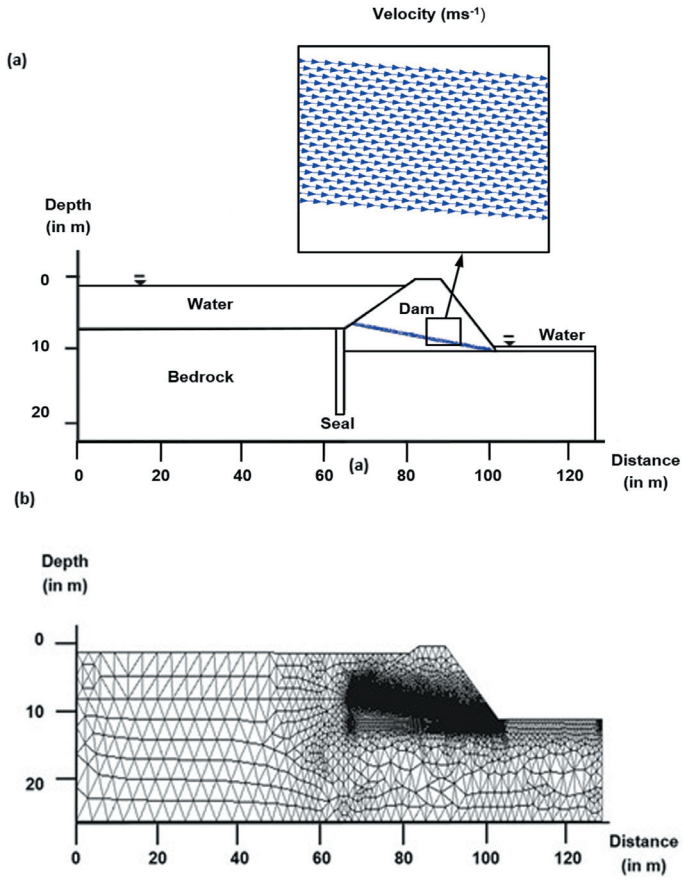

Fig. 5 - Leakage in a dam: a) 2D geometry used for the simulation showing a preferential flow pathway crossing the dam and Darcy velocity map obtained by solving the groundwater flow problem; b) triangular meshes used to discretize the domain for the finite element simulation.

piping sinkholes in the San Vittorino Plain, located in central Italy, along the Velino River Valley. This plain, extensively studied in the past through geological, hydrogeological, geophysical and geochemical surveys, is characterized by the presence of numerous sinkholes, often filled with mineralized spring waters. The development of sinkholes in the study area is mainly due to deep suffusion and deep piping processes, linked to fluid upwelling along fracture-fault systems and to dissolution (by H_2S and CO_2) in the continental deposits (Centamore *et al.*, 2009). The lithology of the geological units is substantially calcareous even if some of them also show a variable alternation of marly-calcareous-cherty layers. The plain, in particular, is characterized by a karst affected carbonate bedrock, arranged in a set of splays with clayey-marly or siliciclastic footwall, whose thickness is estimated to be more than 150 m along the plain. The wide circulation of waters in this area, which includes the presence of the Peschiera Spring system with a relevant discharge rate of about 18 m^3/s, emphasized the action of karst processes.

We developed a 2D synthetic model inspired from this field survey using the finite element forward algorithm described in this work.

We focused only on the results of the ERT and SP line illustrated in Fig. 7, where surface evidence of a piping sinkhole appeared with the formation of a small water pond (around 2.0 m diameter) after about one year from the geophysical measurements. The goal is to verify that negative SP signals are associated with the position of this known sinkhole (this is marked as "A" in Fig. 8).

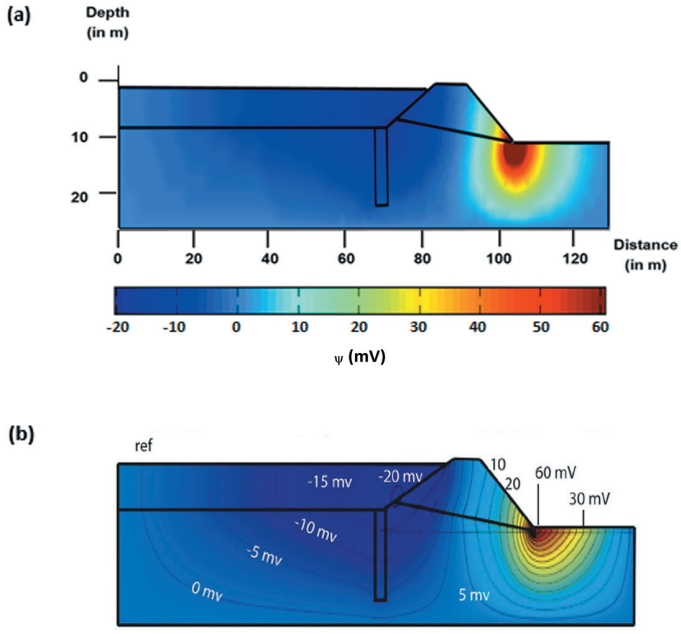

Fig. 6 - SP values from the forward model showing the position of the anomalous flow path through the core of the embankment dam: a) simulation of the self-potential signals using the finite element numerical algorithm with reference at infinity; b) numerical modelling of the synthetic case reported by Ikard *et al*. (2012).

The geological model and the distribution of the electrical conductivity used for the finite element calculation are determined from the 2D ERT profile (Fig. 7a). The values of the hydraulic conductivity for each of the lithological units are the following: 10^{-8} m/s for the upper conductive layer, 10^{-9} m/s for the loamy sand layer and 10^{-7} m/s for the sinkhole (see: Jardani *et al*., 2006a). The geometry used for the computations is shown in Fig. 9. The interfaces between the units are assumed to be flat because the real geometry of this interface has no influence upon the distribution of the electrical potential at the ground surface.

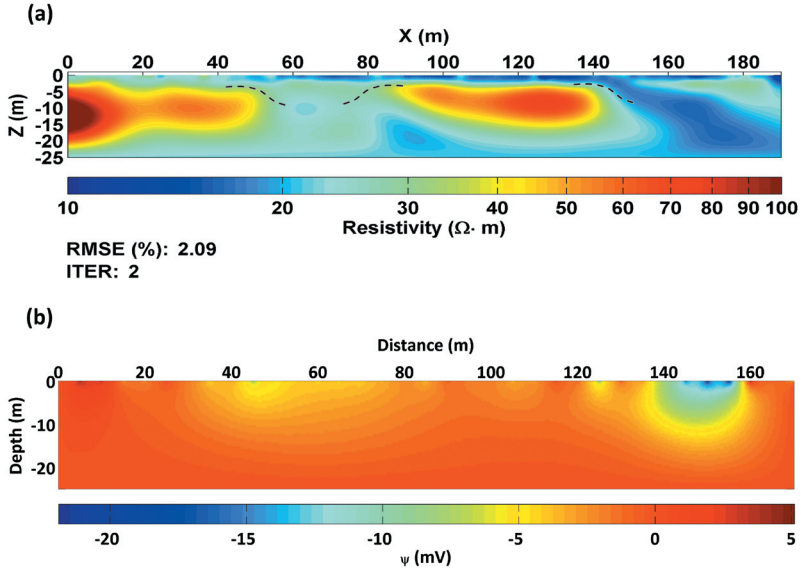

Fig. 7 - Results of the ERT and SP line: a) inverted model of ERT line (after Cardarelli *et al*., 2014); b) SP distribution (in mV) calculated using the finite element numerical algorithm. Model explains well the qualitative features of the observed SP data.

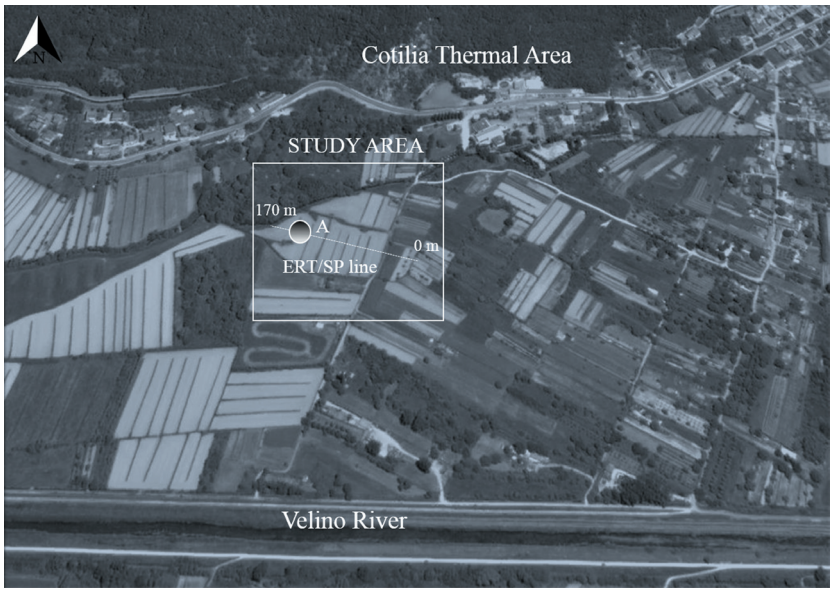

Fig. 8 - Aerial plan of the surveyed area and position of the ERT and SP line.

A pressure source with an amplitude on the order of 10^4 Pa was introduced at the top of the model at the position of the known sinkhole in order to simulate the downflow of the water. The amplitude of the source was chosen by trial and error to fit the observed SP data. This pressure source acts in our model as a ‘‘surrogate’’ force replacing the unknown pressure distribution driving the descent of water from the surface to depth (Byrdina *et al.*, 2009; Bumpus and Kruse, 2014). Instead, at the lower boundary and at the two opposite vertical sides of the system we imposed impermeable boundary conditions. For the electrical potential, we considered $\psi \rightarrow 0$ at infinity (except at the ground surface where $\mathbf{n} \cdot \mathbf{j} = 0$; where $\mathbf{n}$ is the outward unit vector normal to the boundary).

With the characteristics mentioned above, the finite element simulation, shown in Fig. 7, agrees well with the observed SP data collection with RMS = 3 mV (Fig. 10).

As expected, the sinkhole is characterized by a negative anomaly close to the ground surface with respect to a reference electrode taken at infinite because located outside the area where the sinkhole is present. It follows that the SP signatures of the sinkholes are related to the flux of water passing through them. Despite our proposed solution cannot be proven to be unique because the depth and the magnitude of the pressure source are not known a priori, our interpretation offers a good representation of the SP data using electrical resistivity values that have been determined independently.

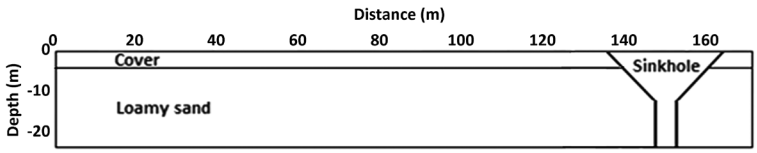

Fig. 9 - Geometrical model used for the finite element calculation. The geological materials are determined from the resistivity tomography.

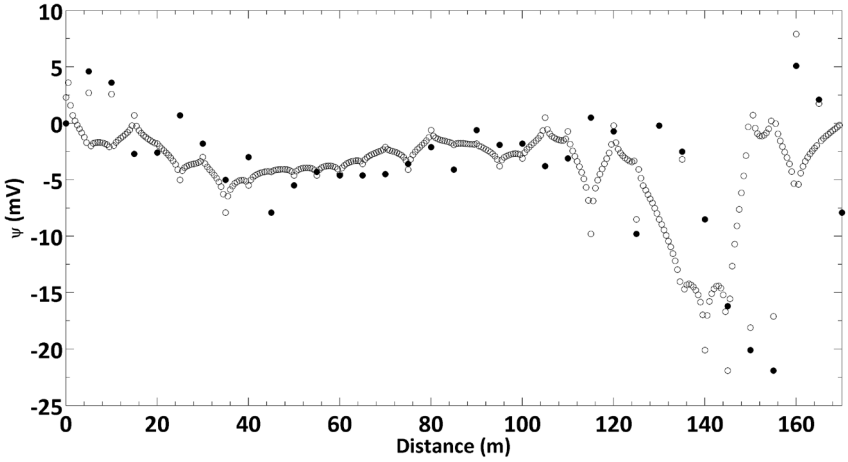

Fig. 10 - Comparison between the SP signals determined at the ground surface using the finite element model (empty circles) and the SP measurements performed along profile (filled circles).

6. Conclusion

We have developed a 2D forward modelling algorithm in Matlab that calculates the SP field induced by fluid flow considering the semi-coupled differential equations of fluid flow and electrical current density.

The main advantage of the proposed code is that it is an open source algorithm. Further, other benefits are that it computes transient or steady state flow models in anisotropic, heterogeneous and water-saturated porous materials and accepts different types of boundary conditions.

The algorithm was used to successfully reproduce the synthetic SP response to a pumping test and seepage through an embankment dam. These two examples clearly demonstrate that the sign and the magnitude of the computed SP signals agrees well with the values of synthetic data obtained by other authors.

Finally, we proposed a finite element model inspired from a field survey in order to compute the SP signals resulting from the infiltration of water into a sinkhole. The distribution of the electrical potential generated by the percolation of the groundwater was determined thanks to the constrains given by the electrical resistivity tomography and SP data. The information about the hydraulic system was inferred from the used simplified geological model.

To explain the observed negative SP anomaly, we assume that the fluid flow is descending. This model offers a good representation of the SP because fairly good agreement is obtained between the computed and the measured SP signals. Nevertheless, the estimate of the numerical parameters of the model is not unique and the magnitude of the pressure source is not known a priori. Despite these limitations, the flow configuration is well constrained and remains the most robust result of our study. Future works will include development of a strategy to solve the inverse problem in order to reconstruct 2D distribution of the source current density responsible of the observed SP anomalies.

Acknowledgements. The present paper was presented at the 35th National Conference of the "Gruppo Nazionale di Geofisica della Terra Solida", held in Lecce from November 22 to 24, 2016.

REFERENCES

Abdelazeem M. and Gobashy M.; 2006: *Self-potential inversion using genetic algorithm*. J. King Abdulaziz Univ., Earth Sci., **17**, 83-101.

Abdelrahman E.M., El-Araby T.M., Hassaneen A.-R.G. and Hafez M.A.; 2003: *New methods for shape and depth determination from SP data*. Geophys., **68**, 1202-1210.

Bastos J.P.A. and Sadowski N.; 2003: *Electromagnetic modelling by finite element methods*. CRC Press, Taylor & Francis Group, New York, NY, USA, 510 pp.

Bear J.; 1988: *Dynamic of fluids in Porous Media*. McGraw-Hill, New York, NY, USA, 764 pp.

Bhattacharya B.B. and Roy N.; 1981: *A note on the use of nomograms for self-potential anomalies*. Geophys. Prospect., **29**, 102-107.

Bumpus P.B. and Kruse S.E.; 2014: *Self-potential monitoring for hydrologic investigations in urban covered-karst terrain*. *Geophys*., **79**, B231-B242.

Butler J.J.; 1988: *Pumping tests in non uniform aquifers - the radially symmetric case*. J. Hydrol., **101**, 15-30.

Byrdina S., Revil A., Contraires S., Pant S., Gautam U., Koirala B., Shrestha P., Tiwari D., Sapkota S. and Perrier F.; 2009: *Dipolar self-potential anomaly associated with carbon dioxide and radon flux at Syabru-Bensi hot springs in central Nepal*. J. Geophys. Res., **114**, B10101.

Cardarelli E., Cercato M., De Donno G. and Di Filippo G.; 2014: *Detection and imaging of piping sinkholes by integrated geophysical methods*. Near Surf. Geophys., **12**, 439-450.

Centamore E., Nisio S. and Rossi D.; 2009: *The San Vittorino Sinkhole Plain: relationships between bedrock structure, sinking processes, seismic events and hydrothermal springs*. Ital. J. Geosci., **128**, 629-639.

De Groot S.R.; 1951: *Thermodynamics of irreversible processes*. North-Holland Publ. Comp., Amsterdam, The Netherlands, 242 pp.

Eppelbaum L.V., Khesin B.E. and Itkis S.E.; 2001: *Prompt magnetic investigations of archaeological remains in areas of infrastructure development: Israeli experience*. Archaeolog. Prospect., **8**, 163-185.

Eppelbaum L.V., Khesin B.E., Itkis S.E. and Ben-Avraham Z.; 2004: *Advanced analysis of self-potential data in ore deposits and archaeological sites*. In: Proc. 10th Eur. Meeting Environ. Eng. Geophys., Utrecht, The Netherlands, pp. 1-4.

Fedi M., Cella F., Quarta T. and Villani A.V.; 2010: *2D continuous wavelet transform of potential fields due to extended source distributions*. Appl. Comput. Harmon. Anal., **28**, 320-337.

Ikard S.J., Revil A., Jardani A., Woodruff W.F., Parekh M. and Mooney M.; 2012: *Saline pulse test monitoring with the self-potential method to non-intrusively determine the velocity of the pore water in leaking areas of earth dams and embankments*. Water Resour. Res., **48**, W04201.

Ishido T. and Mizutani H.; 1981: *Experimental and theoretical basis of electrokinetic phenomena in rock-water systems and its applications to geophysics*. J. Geophys. Res., **86**, 1763-1775.

Iuliano T., Mauriello P. and Patella D.; 2002: *Looking inside Mount Vesuvius by potential fields integrated probability tomographies*. J. Volcanol. Geotherm. Res., **113**, 363-378.

Jardani A., Dupont J.P. and Revil A.; 2006a: *Self-potential signals associated with preferential groundwater flow pathway sinsinkholes*. J. Geophys. Res., **111**, B09204.

Jardani A., Revil A. and Dupont J.P.; 2006b: *Self-potential tomography applied to the determination of cavities*. Geophys. Res. Lett., **33**, L13401.

Jardani A., Revil A., Bolève A., Dupont J.P., Barrash W. and Malama B.; 2007a: *Tomography of groundwater flow from self-potential (SP) data*. Geophys. Res. Lett., **34**, L24403.

Jardani A., Revil A., Santos F., Fauchard C. and Dupont J.P.; 2007b: *Detection of preferential infiltration pathways in sinkholes using joint inversion of self-potential and EM-34 conductivity data*. Geophys. Prospect., **55**, 1-11.

Linde N. and Revil A.; 2007: *Inverting residual self-potential data for redox potentials of contaminant plumes*. Geophys. Res. Lett., **34**, L14302.

Louwyck A., Vandenbohede A., Bakker M. and Lebbe L.; 2012: *Simulation of axi-symmetric flow towards wells: a finite-difference approach*. Comput. Geosci., **44**, 136-145.

Meiser P.; 1962: *A method of quantitative interpretation of self-potential measurements*. Geophys. Prospect., **10**, 203-218.

Mendonça C.A.; 2008: *Forward and inverse self-potential modelling in mineral exploration*. Geophys., **73**, F33-F43.

Minsley B.J.; 2007: *Modelling and inversion of self-potential data*. PH.D. Thesis in Geophysics, Massachusetts Institute of Technology, Cambridge, MA, USA, 251 pp.

Mitchell J.K.; 1991: *Conduction phenomena: from theory to geotechnical practice*. Geotech., **43**, 299-340.

Onsager L.; 1931: *Reciprocal relations in irreversible processes. I.* Phys. Rev., **37**, 405-426.

Peksen E., Yas T., Kayman A.Y. and Ozkan C.; 2011: *Application of particle swarm optimization on self-potential data*. J. Appl. Geophys., **75,** 305-318.

Revil A. and Jardani A.; 2010: *Stochastic inversion of permeability and dispersivities from time lapse self-potential measurements: a controlled sandbox study*. Geophys. Res. Lett., **37**, L11404.

Revil A. and Linde N.; 2006: *Chemico-electromechanical coupling in microporous media*. J. Colloid Interface Sci., **302**, 682-694.

Sheffer M.R. and Oldenburg D.W.; 2007: *Three-dimensional modelling of streaming potential*. Geophys. J. Int., **169**, 839-848.

Shi W.; 1998: *Advanced modelling and inversion techniques for three-dimensional geoelectrical surveys*. PH.D. Thesis in Geophysics, Massachusetts Institute of Technology, Cambridge, MA, USA, 210 pp.

Sill W.R.; 1983: *Self-potential modelling from primary flows*. Geophys., **48**, 76-86.

Soueid Ahmed A., Jardani A., Revil A. and Dupont J.P.; 2013: *SP2DINV: a 2D forward and inverse code for streaming potential problems*. Comput. Geosci., **59**, 9-16.

Srivastava R.P. and Sen M.K.; 2009: *Fractal based stochastic inversion of poststack seismic data using very fast simulated annealing*. J. Geophys. Eng., **6**, 412-425.

Stoll J., Bigalke J. and Grabner E.W.; 1995: *Electrochemical modeling of self-potential anomalies*. Surveys in Geophysics, **16**, 107-120.

Theis C.V.; 1935: *The relation between the lowering of the piezometric surface and the rate and duration of discharge of a well using ground-water storage*. Am. Geophys. Un. Trans., **16**, 519-524.

Titov K., Revil A., Konosavsky P., Straface S. and Troisi S.; 2005: *Numerical modelling of self potential signals associated with a pumping test experiment*. Geophys. J. Int., **162**, 641-650.

Appendix

In this appendix, we show the assembly process which is at the heart of the finite element method. Local, global Stiffness and Mass matrices and right hand side are all computed by the function **FEM_static.m** whether we use stationary simulations. This function, which is listed below, is structured as illustrated in Fig. 1a.

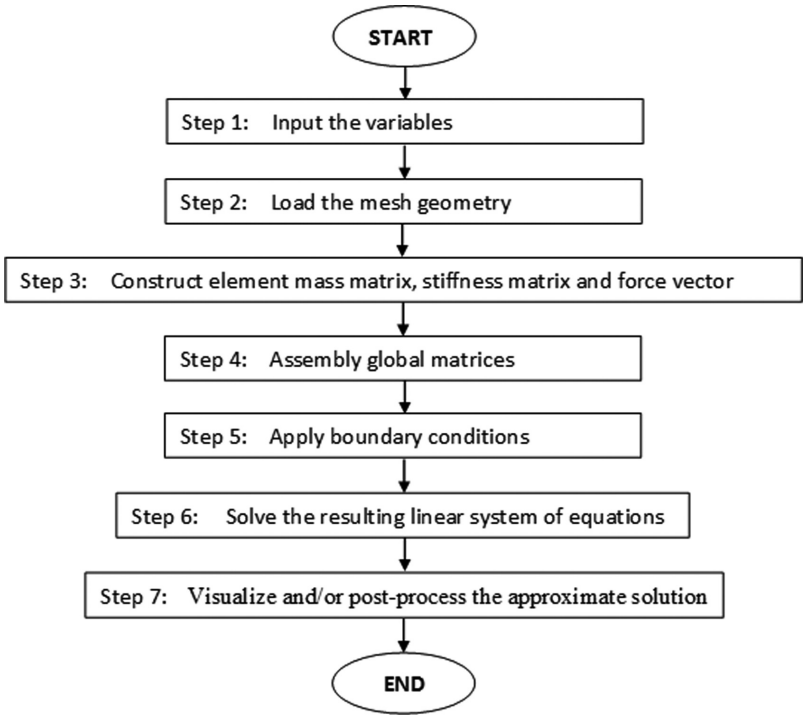

Fig. 1a - The structure of the MatLAB function:
function (A, b, u) = FEM_static (Q, node, elem, Dirichlet, Neumann, S);

```
% Input;
% Q: sink source;
% node: node coordinates;
% elem: mesh connectivities;
% Dirichlet, Neumann: boundary edges;
% K: in the case of ground water flow, it represents hydraulic conductivity % in the case of electrical potential, it
represents electrical conductivity;
%
%
% Output:
% u: solution of the problem;
% A: stiffness matrix;
% b: right-hand side;
N = size (node, 1);
A = sparse (N, N); u = zeros (N, 1); b = sparse (N, 1);
(fs) = centre (Q, node, elem); % gives the value of Q in the centre of gravity of each element
%% Assembling stiffness matrix
% The function local.m calculates the local stiffness matrix using the coordinates % of the vertices of the corresponding
element.
for j = 1 : size (elem, 1)
A [elem (j, :), elem (j, :)] = A [elem (j, :), ...
elem (j, :)] + {{local {node [elem (j, :), :]} * K (j)}};
end
%% Assembling right side
for j = 1 : size (elem, 1)
b [elem (j, :)] = b [elem (j, :)] + ...
det {{1, 1, 1; node [elem (j, :), :] ‘ }} * ...
fs (j) /6 ;
end
%% Neumann boundary conditions
% The function nd.m is called with the coordinates of points on the Neumann
% boundary and returns values of the normal-derivative at N discrete points on
% the Neumann boundary
if [~ is empty (Neumann)]
der = sqrt {{sum {[node (Neumann (:, 1), :] – node [Neumann (:, 2), :]}. ^ 2, 2}};
centre = {node [Neumann (:, 1), :] + node [Neumann (:, 2), :]} / 2;
b = b + accumarray {Neumann (:), repmat [der. * nd (center) / 2, 2, 1], (N, 1)};
end
%% Dirichlet boundary conditions
% The function dv.m is called with the coordinates of points on the Dirichlet
% boundary and returns values at the corresponding locations
isBdNode = false (N, 1);
if ~isempty (Dirichlet)
isBdNode [Dirichlet (:)] = true;
u (isBdNode) = dv [node (isBdNode, :)];
b = b - A * u;
else % Pure Neumann boundary condition
b = b - mean (b);
isBdNode (1) = true;
end
%% Solve Au = b
freeNode = find (~isBdNode);
u (freeNode) = A (freeNode, freeNode) \ b (freeNode).
```

Corresponding author: Ilaria Oliveti
Universita degli Studi La Sapienza, Facolta di Ingegneria Civile e Industriale
Via Eudossiana 18, 00184 Rome, Italy
Phone: +39 06 44 585 076; e-mail: ilaria.oliveti@uniroma1.it